

Journal of Astronomical Telescopes, Instruments, and Systems

AstronomicalTelescopes.SPIEDigitalLibrary.org

MuSCAT: a multicolor simultaneous camera for studying atmospheres of transiting exoplanets

Norio Narita
Akihiko Fukui
Nobuhiko Kusakabe
Masahiro Onitsuka
Tsuguru Ryu
Kenshi Yanagisawa
Hideyuki Izumiura
Motohide Tamura
Tomoyasu Yamamuro

MuSCAT: a multicolor simultaneous camera for studying atmospheres of transiting exoplanets

Norio Narita,^{a,b,c,*} Akihiko Fukui,^d Nobuhiko Kusakabe,^b Masahiro Onitsuka,^{b,c} Tsuguru Ryu,^{b,c} Kenshi Yanagisawa,^d Hideyuki Izumiura,^{c,d} Motohide Tamura,^{a,b,e} and Tomoyasu Yamamuro^f

^aAstrobiology Center, National Institutes of Natural Sciences, 2-21-1 Osawa, Mitaka, Tokyo 181-8588, Japan

^bNational Astronomical Observatory of Japan, 2-21-1 Osawa, Mitaka, Tokyo 181-8588, Japan

^cSOKENDAI (The Graduate University of Advanced Studies), 2-21-1 Osawa, Mitaka, Tokyo 181-8588, Japan

^dOkayama Astrophysical Observatory, National Astronomical Observatory of Japan, Kamogata, Asakuchi, Okayama 719-0232, Japan

^eThe University of Tokyo, Department of Astronomy, 7-3-1 Hongo, Bunkyo-ku, Tokyo 113-0033, Japan

^fOptCraft, 3-16-8 Higashi-Hashimoto, Midori-ku, Sagami-hara, Kanagawa 252-0144, Japan

Abstract. We report a development of a multicolor simultaneous camera for the 188-cm telescope at Okayama Astrophysical Observatory in Japan. The instrument, named MuSCAT (Multicolor Simultaneous Camera for studying Atmospheres of Transiting exoplanets), has a capability of three-color simultaneous imaging in optical wavelengths where CCDs are sensitive. MuSCAT is equipped with three 1024×1024 pixel CCDs which can be controlled independently. The three CCDs detect lights in g'_2 (400 to 550 nm), r'_2 (550 to 700 nm), and $z'_{s,2}$ (820 to 920 nm) bands using Astrodon Photometrics Generation 2 Sloan filters. The field of view of MuSCAT is 6.1×6.1 arc min² with the pixel scale of 0.358 arc sec /pixel. The principal purpose of MuSCAT is to perform high-precision multicolor transit photometry. For this purpose, MuSCAT has the capability of self-autoguiding which enables it to fix the positions of stellar images within ~ 1 pixel. We demonstrate relative photometric precisions of 0.101%, 0.074%, and 0.076% in g'_2 , r'_2 , and $z'_{s,2}$ bands, respectively, for GJ 436 (magnitudes in $g' = 11.81$, $r' = 10.08$, and $z' = 8.66$) with 30-s exposures. The achieved precisions meet our objective, and the instrument is ready for operation. © The Authors. Published by SPIE under a Creative Commons Attribution 3.0 Unported License. Distribution or reproduction of this work in whole or in part requires full attribution of the original publication, including its DOI. [DOI: [10.1117/1.JATIS.1.4.045001](https://doi.org/10.1117/1.JATIS.1.4.045001)]

Keywords: instrumentation; exoplanets; multicolor; photometry; transits.

Paper 15019 received Apr. 28, 2015; accepted for publication Jul. 16, 2015; published online Aug. 27, 2015.

1 Introduction

Transiting planets, which transit in front of their host stars, are especially important research objects among exoplanets, because when combined with radial velocity measurements, they can provide us various information about the nature of exoplanets such as the mass, radius, density, orbital obliquity, and atmosphere. Most of the transiting planets have been discovered by transit surveys which monitor the brightness of hundreds of thousands of stars. Several groups have worked or been working on ground-based transit surveys,^{1–3} and CoRoT⁴ and Kepler⁵ have performed space-based transit surveys. Moreover, the second epoch mission of Kepler, namely K2,⁶ is now in operation, and next generation space missions TESS⁷ and PLATO⁸ have been approved to be launched around 2017 and 2024, respectively.

The biggest problem for transit surveys, especially for ground-based ones, is the commingling of false positives with candidates of transiting planets. The cause of false positives of transiting planets is eclipsing binaries, as they mimic planetary transits by grazing or by being mixed in another bright star's brightness. Thus, it is important to conduct follow-up observations after transit surveys in order to validate candidates as true planets by eliminating false positives.

High-precision multicolor transit photometry is known to be useful for such follow-up observations to discriminate whether transit-like dimming is caused by a true planet or by an eclipsing

binary.⁹ This is because a true planet is almost dark in all wavelengths, while the intervening body of an eclipsing binary is bright itself and its brightness changes significantly with wavelength. Thus, false positives caused by eclipsing binaries can be spotted by observing the significant wavelength dependence in transit depths. On the other hand, transit depths of a true planet also have wavelength dependence. Most of the wavelength dependence comes from the stellar limb darkening, but the apparent planetary radius also has a weak wavelength dependence which reflects the nature of its planetary atmosphere. High-precision multicolor transit photometry is known to be useful to measure the weak wavelength dependence in transit depths to study atmospheres of transiting planets. This kind of study is known as transmission spectroscopy, and multiple numbers of multicolor transit observations for this purpose have been reported so far.^{10–17}

Multicolor simultaneous cameras are very fruitful for the studies described above for two reasons. First, multicolor simultaneous cameras provide not only higher efficiency but also more feasibility to accomplish the study objectives than single-color cameras, since observable transits from a specific ground site are very limited. Second, simultaneity of multicolor transit photometry is important to avoid systematic differences of transit depths due to luminosity changes in host stars possibly caused by the existence of starspots, plagues, stellar activity, and so on. For these reasons, multicolor simultaneous cameras such as GROND,^{10,11} BUSCA,¹² ULTRACAM,¹³ SIRIUS,^{14,15} and MITSuME^{16,17} have been actively used for transit observations.

*Address all correspondence to: Norio Narita, E-mail: norio.narita@nao.ac.jp

Considering the fact that more interesting transiting planets will be discovered in the near future by advanced ground-based surveys and also by space-based surveys such as K2, TESS, and PLATO, developments of new multicolor simultaneous cameras are highly desired. We report here the development of such an astronomical instrument named MuSCAT (Multicolor Simultaneous Camera for studying Atmospheres of Transiting exoplanets), which is now installed on the 188-cm telescope at Okayama Astrophysical Observatory (OAO) in Japan.

The rest of this paper is organized as follows. We first describe designs of the optical system of MuSCAT and its components (Sec. 2) and introduce the control system of MuSCAT (Sec. 3). We then report characteristics and performances of MuSCAT shown in engineering observations (Sec. 4). We discuss some capabilities for a future upgrade of MuSCAT (Sec. 5), and finally summarize this paper (Sec. 6).

2 Optical System

2.1 Scientific Requirements and Design Policies

We have designed MuSCAT considering the following conditions. As we plan to use MuSCAT for validations of transiting planets discovered by transit surveys, at least two colors are necessary to discriminate eclipsing binaries from transiting planets. Considering the cost and available research grants, we adopt a design for a three-color simultaneous camera with the three colors in optical wavelengths where CCDs are sensitive. For transit observations, it is important to obtain good comparison stars in the field of view (FOV) to achieve high-precision transit photometry. For this reason, we have designed the MuSCAT FOV as wide as possible for the 188-cm telescope. We have also taken care of the throughput (TP) of the instrument to achieve high photometric precision. To achieve high sensitivity to the utmost extent, we have carefully selected and designed the MuSCAT

optical system including astronomical bandpass filters, dichroic mirrors, and CCDs.

2.2 Optical Design

Layouts of the optical system of MuSCAT are shown in Fig. 1. MuSCAT adopts a 45 deg plane mirror and an Offner relay, which consist of SiO_2 -protected aluminum mirrors, and inserts two dichroic mirrors in the light path to simultaneously take images of three bands in optical wavelengths. MuSCAT maintains space for another dichroic mirror around the Cassegrain focus so as to accommodate near-infrared (NIR) channels as a future upgrade capability. For high-precision transit photometry, it is desirable to have the widest possible FOV to get good comparison stars. The Offner relay enables us to distribute F conversion lenses around the relay. The lenses contribute to achieve a wider FOV by converting the F-number from F18 at the telescope to F5.5 before the relay and further converting to F4.0 just before the CCD cameras after the relay. Aberration correction is performed by four lenses before and one lens after the Offner relay, and is finally accomplished by a plane-convex lens just before the CCD cameras. An antireflection coating for optical wavelength is applied to the lenses. The lenses are designed to correct the aberration of the whole system including both the 188-cm telescope and MuSCAT. Thereby, the optical system of MuSCAT provides a good imaging quality throughout the FOV. Wavelength divisions are performed by two dichroic mirrors after the Offner relay. The dichroic mirrors are wedge-shaped to reduce astigmatism. Astronomical bandpass filters are inserted just before the last lenses. Lights of astronomical objects are divided into three colors and detected by three CCD cameras. A picture of the actual MuSCAT installed on the 188-cm telescope is presented in Fig. 2.

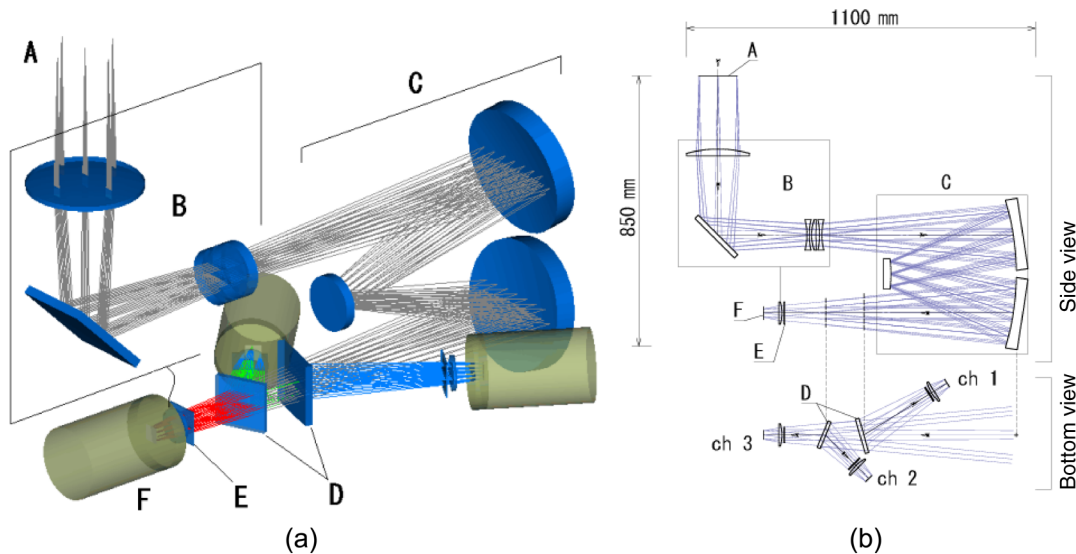


Fig. 1 Layouts of the optical system of multicolor simultaneous camera for studying atmospheres of transiting exoplanets (MuSCAT): (a) in three-dimensional and (b) in two-dimensional. Meanings of the labels in the panels are as follows. (A) Telescope focal plane (126 to 126 mm); (B) F conversion optics, constructed in order with S-BSL7 lens, 45 deg mirror, CaF₂ lens, S-LAL8 lens, CaF₂ lens, and finally BK7 lens after bandpass filters in front of detectors; (C) Offner relay; (D) dichroic mirrors; (E) bandpass filters; and (F) detectors. The vertical dashed lines in panel (b) indicate the same positions, but the bottom shows a view from the bottom.



Fig. 2 A picture of MuSCAT installed on the 188-cm telescope.

2.3 Dichroic Mirrors and Bandpass Filters

The two dichroic mirrors are manufactured by Asahi Spectra Co., Ltd. The size of the first dichroic mirror (DM1) is 113 mm × 108 mm, and the depth is 11.8 mm with a wedge angle of 7 min 52 s. The size of the second dichroic mirror (DM2) is 90 mm × 88 mm with a depth of 9.9 mm and a wedge angle of 12 min 33 s. An antireflection coating is processed on the back sides of the dichroic mirrors so that the DMs transmit the remaining lights (namely, not reflected ones) almost completely. Figure 3 plots the wavelength dependence of reflectance of DM1 and DM2 measured by a goniospectrophotometer. The reflectance of both DMs is almost flat across the relevant wavelength for the three bands. We note that there are wiggles in the reflectance around 350 nm for both DMs and around 525 nm for the DM2, but those wiggles do not affect the three current bands.

The DM1 is inserted with an incident angle of 16 deg and it reflects most of the light in 400 to 550 nm and transmits the remaining light past 550 nm. Reflected light from the DM1 is detected by the ch 1 CCD camera. Then the DM2 is inserted with an incident angle of 22.5 deg and it reflects most of the light in the 550 to 700 nm range and transmits the remaining light

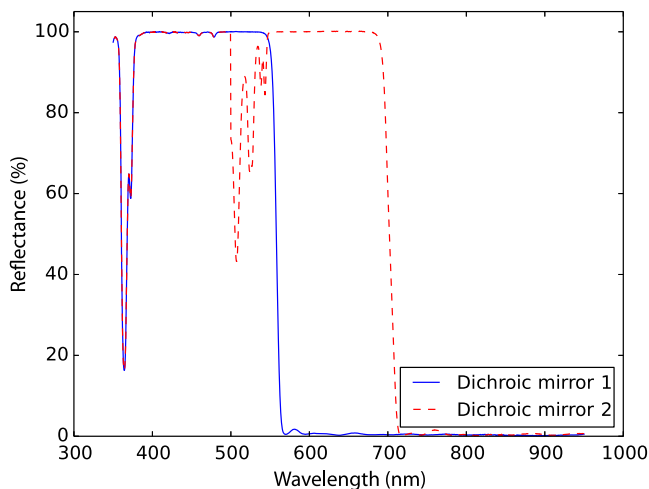


Fig. 3 Wavelength dependence of reflectances of DM1 and DM2.

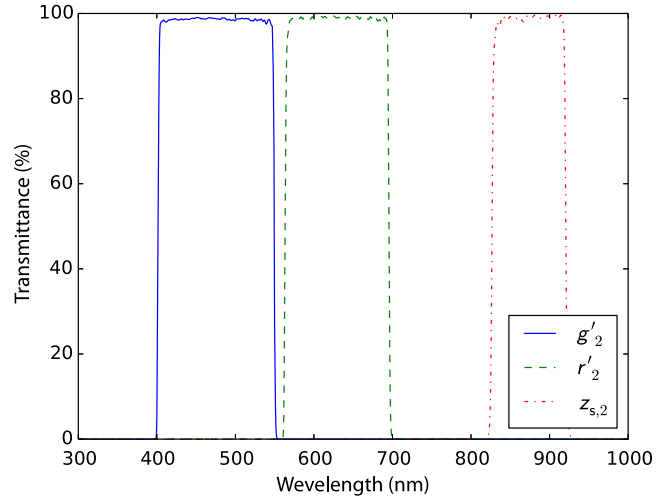


Fig. 4 Wavelength dependence of transmittances of bandpass filters.

past 700 nm. The reflected light from the DM2 is detected by the ch 2 CCD camera, and the transmitted light from the DM2 is detected by the ch 3 CCD camera.

We adopt the g'_2 , r'_2 , and $z_{s,2}$ band filters of Astrodon Photometrics Generation 2 Sloan filters. The size of those filters is 50 mm × 50 mm. Figure 4 plots the wavelength dependence of the transmittance of the bandpass filters, measured by a spectrophotometer SHIMADZU UV-3100PC. The reflectance and transmittance of DM1 and DM2 are optimized for those three bands.

We note that changes in the reflectance and transmittance of DMs and bandpass filters are negligible in normal operations unless dew condensation occurs.

2.4 Cameras and Detectors

MuSCAT equips three CCD cameras manufactured by Princeton Instruments. The first one is a PIXIS: 1024B model, used as the ch 2 CCD camera in the r'_2 band. The other two are PIXIS: 1024B_eXcelon model cameras, used as the ch 1 (g'_2 band) and ch 3 ($z_{s,2}$ band) CCD cameras. Each CCD camera is equipped with a back-illuminated grade 1 CCD chip (e2v CCD47-10 for PIXIS: 1024 and Princeton Instruments' proprietary CCD for PIXIS: 1024B_eXcelon) with 1k × 1k (1024 × 1024) pixels. It is noted that the CCDs of PIXIS: 1024B_eXcelon, are specially processed to suppress the etaloning (fringing) that occurs in standard back-illuminated CCDs. Quantum efficiencies (QEs) of PIXIS: 1024B and PIXIS: 1024B_eXcelon are plotted in Fig. 5. A special broadband antireflection coating (BBAR coating) is applied to the vacuum windows of CCD cameras and its transmittance is shown in Fig. 6. The data of the QEs and the transmittance of the BBAR coating are provided by the manufacturer. We summarized nominal specifications of the CCD cameras in Table 1. We also presented actual measured values of gains, full well, and read noise as well as an upper limit of dark current based on data taken during engineering observations (Sec. 4) in Table 1.

2.5 Total Throughput

Efficiencies of the F conversion optics and the Offner relay are roughly estimated as 60% in the g'_2 band, 61% in the r'_2 band, and 50% in the $z_{s,2}$ band. Based on the transmittance and reflectance of DMs, filters, BBAR coating, and QE of CCDs, in

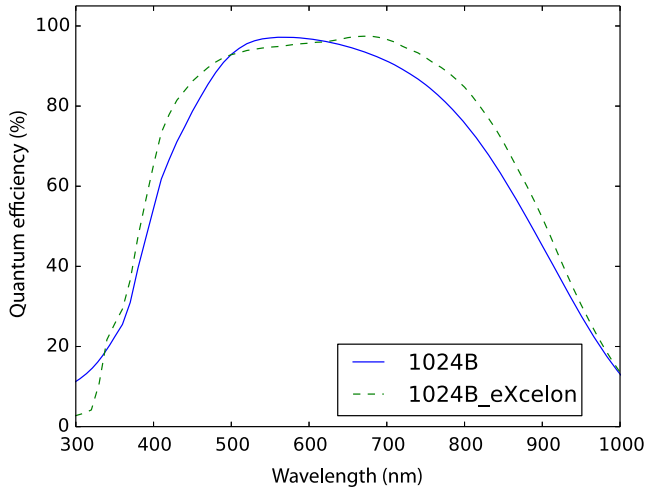


Fig. 5 Wavelength dependence of quantum efficiency of CCDs.

Sec. 2.4, we calculate the expected total TP of MuSCAT. We plot the wavelength dependence of the expected total TP of MuSCAT in Fig. 7 and present the machine-readable values in Table 2. A comparison of the expected total TP with the measured one is presented in Sec. 4.3.

2.6 Field of View

MuSCAT has a 6.1×6.1 arc min² FOV with the $1k \times 1k$ CCDs introduced above. The pixel scale for each CCD is ~ 0.358 arc sec/pixel (see Fig. 18 for details). Centers of the FOVs of three CCD cameras are adjusted within 10 pixels in both the x - and y -directions, and relative rotations of the position angle are fit within 1 deg.

As a future upgrade capability, MuSCAT can replace CCD cameras with $2k \times 2k$ (2048×2048 pixels) CCD cameras PIXIS: 2048B and PIXIS: 2048B_eXcelon. With such an upgrade, the FOV of MuSCAT will increase to 12.7×12.7 arc min². In that case, the small (0% to 4%) vignetting depending on the wavelength would occur in the region outside the diameter of 14.4 arc min from the center of the FOV, while there is no vignetting for the $1k \times 1k$ CCDs. Figure 8 indicates the explained potential FOV of MuSCAT.

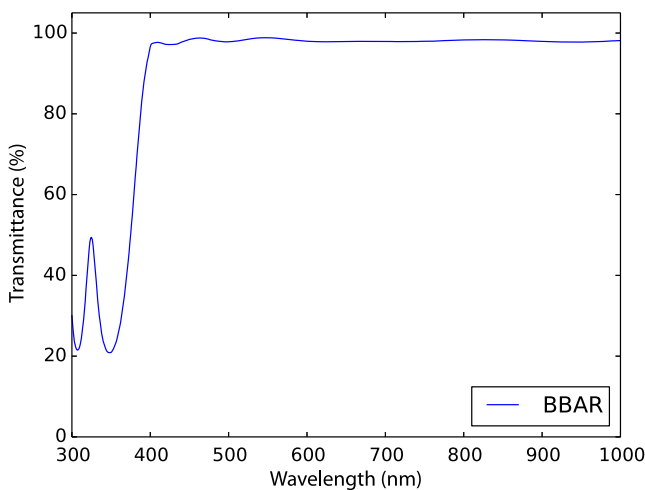


Fig. 6 Wavelength dependence of transmittance of broadband anti-reflection coating.

Table 1 Summary of basic information of cameras and CCDs.

Camera name	PIXIS 1024B/PIXIS 1024B_eXcelon
CCD format	1024 × 1024 pixels
Pixel size	13 × 13 μm
Imaging area	13.3 × 13.3 mm
Data interface	USB2.0
Dimensions	16.59 cm × 11.81 cm × 11.38 cm (L × W × H)
Weight	2.27 kg
Selectable gain modes	1, 2, 4 e ⁻ /ADU
Measured gains:	
Mode 1	1.00 (ch 1), 1.02 (ch 2), 1.00 (ch 3) e ⁻ /ADU
Mode 2	1.98 (ch 1), 2.02 (ch 2), 2.00 (ch 3) e ⁻ /ADU
Mode 4	3.96 (ch 1), 4.05 (ch 2), 3.97 (ch 3) e ⁻ /ADU
Dark current at -70°C	<0.0015e ⁻ s ⁻¹ pixel ⁻¹ (measured) 0.0004e ⁻ s ⁻¹ pixel ⁻¹ (catalog typical value)
Full well:	
Single pixel	~70,000e ⁻
Selectable readout speed (readout time)	100 kHz (10.0 s), 2 MHz (0.58 s)
Measured read noise:	
At 100 kHz	3.9 (ch 1), 3.8 (ch 2), 4.2 (ch 3) e ⁻
At 2 MHz	11 (ch 1), 12 (ch 2), 24–27 ^a (ch 3) e ⁻

^aAn additional pattern (not random) noise is seen only in the 2 MHz mode of the ch 3 CCD. This is scheduled to be repaired (the repair has been completed at the time of publication).

2.7 Spot Diagram

Simulated imaging performances of the MuSCAT optical system are shown in spot diagrams in Figs. 9 and 10. Figure 9 plots spot diagrams for on-focus cases which indicate that the spot radii of all wavelengths are well under 1 arc sec throughout the current FOV and the potential FOV. This imaging performance is thus sufficient for the OAO where the typical region observed is about 1.5 arc sec. Figure 10 shows spot diagrams for defocused cases where the secondary mirror is shifted by 1.5 mm, which makes the spot radius expand to about 4 arc sec. It is well known that defocusing is very useful for high-precision transit photometry for isolated sources,¹⁸ thus those cases are more realistic for transit observations. The panels imply that images are almost circular throughout the FOV and are suitable for aperture photometry.

Table 2 Wavelength dependence of expected total efficiencies of multicolor simultaneous camera for studying atmospheres of transiting exoplanets (MuSCAT).

Wavelength (nm)	g'_2 (%)	r'_2 (%)	$z_{s,2}$ (%)	Wavelength (nm)	g'_2 (%)	r'_2 (%)	$z_{s,2}$ (%)
360	0.00	0.00	0.00	660	0.00	55.37	0.00
370	0.00	0.00	0.00	670	0.00	54.80	0.00
380	0.00	0.00	0.00	680	0.00	54.35	0.00
390	0.00	0.00	0.00	690	0.00	52.67	0.00
400	2.02	0.00	0.00	700	0.00	0.07	0.00
410	42.21	0.00	0.00	710	0.00	0.00	0.00
420	44.63	0.00	0.00	720	0.00	0.00	0.00
430	46.75	0.00	0.00	730	0.00	0.00	0.00
440	48.39	0.00	0.00	740	0.00	0.00	0.00
450	50.36	0.00	0.00	750	0.00	0.00	0.00
460	50.99	0.00	0.00	760	0.00	0.00	0.00
470	52.42	0.00	0.00	770	0.00	0.00	0.00
480	52.35	0.00	0.00	780	0.00	0.00	0.00
490	53.23	0.00	0.00	790	0.00	0.00	0.00
500	53.56	0.00	0.00	800	0.00	0.00	0.00
510	54.21	0.00	0.00	810	0.00	0.00	0.00
520	54.45	0.00	0.00	820	0.00	0.00	0.08
530	54.87	0.00	0.00	830	0.00	0.00	35.05
540	54.58	0.00	0.00	840	0.00	0.00	36.12
550	15.81	0.00	0.00	850	0.00	0.00	34.50
560	0.00	0.06	0.00	860	0.00	0.00	32.74
570	0.00	57.17	0.00	870	0.00	0.00	30.78
580	0.00	56.60	0.00	880	0.00	0.00	29.08
590	0.00	57.07	0.00	890	0.00	0.00	27.13
600	0.00	56.74	0.00	900	0.00	0.00	25.21
610	0.00	56.73	0.00	910	0.00	0.00	22.99
620	0.00	56.56	0.00	920	0.00	0.00	14.40
630	0.00	56.29	0.00	930	0.00	0.00	0.02
640	0.00	55.97	0.00	940	0.00	0.00	0.00
650	0.00	55.63	0.00	950	0.00	0.00	0.00

3 Control System

3.1 System Structure

Figure 11 shows a flowchart of the MuSCAT control system. The system consists of two personal computers: one (PC1) is

directly mounted on the instrument and the other (PC2) is located in an observation room in the observatory. We use Linux/CentOS 5 (32 bit) for PC1 and Linux/CentOS 7 (64 bit) for PC2. For PC1, a 32 bit operating system is required to customize observation commands using a 32 bit library for

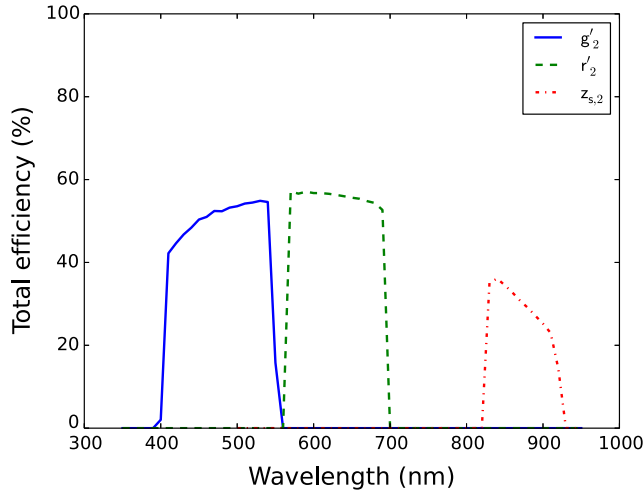


Fig. 7 Wavelength dependence of expected total efficiencies of MuSCAT in g'_2 , r'_2 , and $z_{s,2}$ bands.

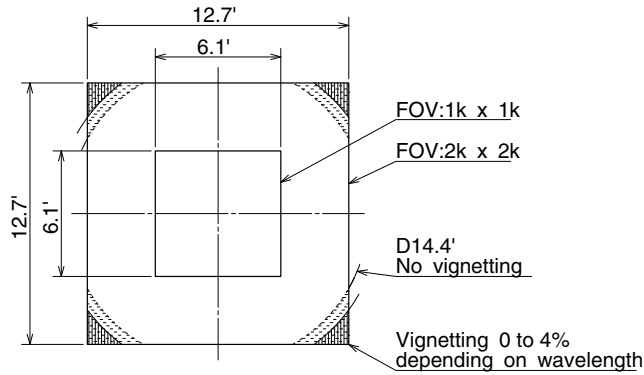


Fig. 8 A schematic view of the potential field of view (FOV) of MuSCAT.

the CCD cameras. Those operating systems may be subject to change in the future.

Each of the CCD cameras is connected to PC1 with a USB cable. Each camera is independently controlled by PC1 using an interface software which is developed based on PVCAM and CFITSIO C libraries. The images taken by these cameras are saved in a 16-bit FITS format along with FITS header information including the time information, telescope status, dome status, and weather information. For the time information, PC1 refers to the internal clock which is synchronized to Network Time Protocol servers via the internet. The typical time offset between the local machine and the NTP servers is less than 1 ms. Thus, the total systematic uncertainties on the times of exposures, including the time lag between the internal time acquisition and actual exposure, are well within 1 s, which are negligible for even time-critical sciences such as transit timing measurements. For information other than the time, PC1 refers to a telescope-control PC, which gathers all the up-to-the-second information.

PC2 provides a user interface. Observers can send an observing command to each camera from this PC specifying the exposure time, number of images, gain and readout speed settings, and so on. We note that one can select optimal settings for each camera. Namely, one can set a different exposure time and a different readout speed for each camera. This is an important feature of MuSCAT, that an optimal exposure time can independently be used for each band. The observed images are instantaneously sent to PC2 to be displayed in SAOImage DS9. PC2 also has a function of self-autoguiding (see Sec. 3.2), and has data storage.

3.2 Self-Autoguiding

To achieve a 0.1% level high-precision relative photometry, it is essential to receive stellar fluxes by the same pixels during a set of observations to mitigate the incompleteness of the pixel-to-pixel sensitivity correction. Because the tracking of the 188-cm telescope is not perfect, an autoguiding system is critical to keep the stars in the same positions on the detectors. However,

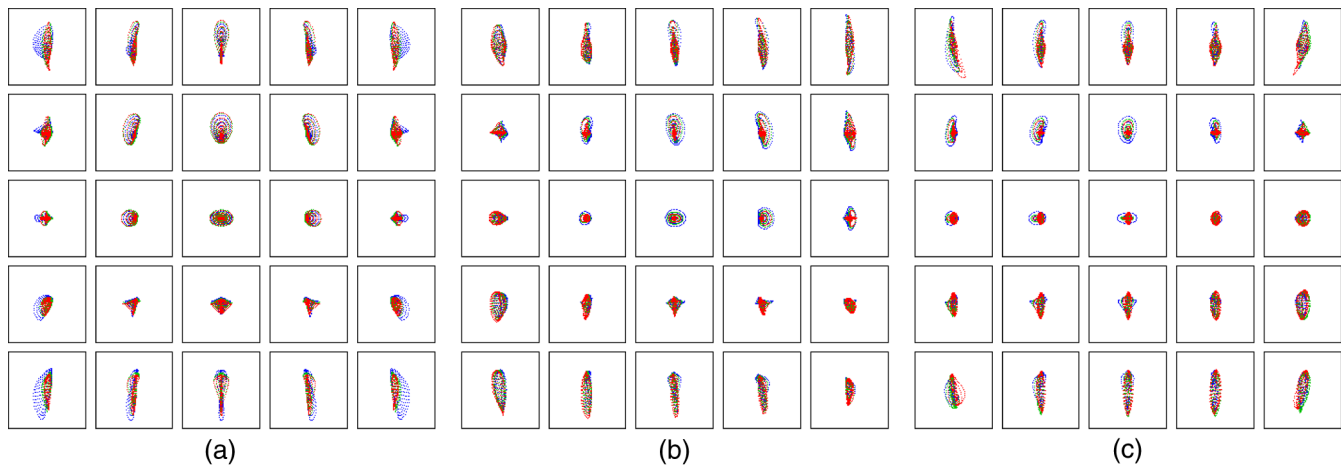


Fig. 9 Spot diagram of the CCD cameras for on-focus cases for (a) ch 1, (b) ch 2, and (c) ch 3. The 5×5 pixel cells represent the FOV of the $2k \times 2k$ CCD case, while the inner 3×3 pixel cells represent for the FOV of the $1k \times 1k$ CCD. The size of each cell corresponds to 2×2 arc sec. Colors indicate simulated images of the shortest (blue), mid (green), and longest (red) wavelength in each channel. Specifically, 400, 470, and 550 nm for ch 1; 550, 630, and 700 nm for ch 2; and 700, 800, and 950 nm for ch 3.

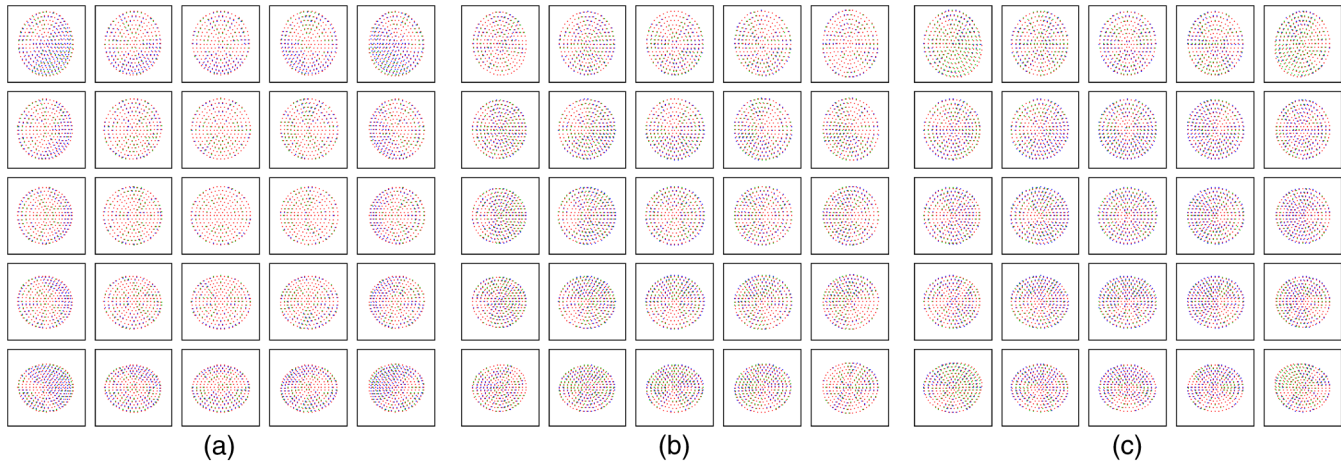


Fig. 10 Same as Fig. 9, but for defocused cases. The size of each cell corresponds to 10×10 arc sec.

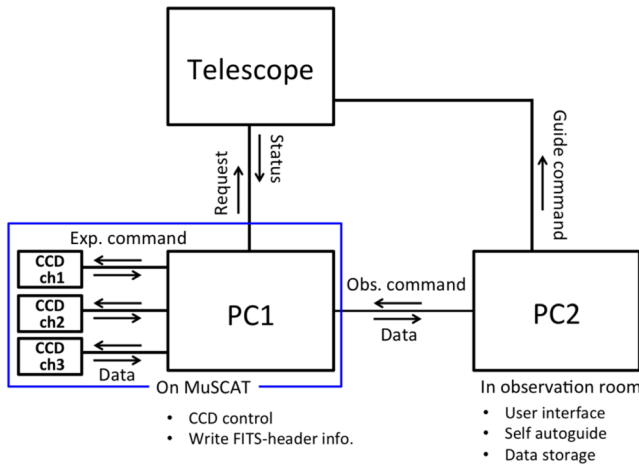


Fig. 11 A flowchart of MuSCAT control system.

MuSCAT has no guide camera to capture a guide star located in the surrounding area of the FOV of the science cameras. We, therefore, have developed a self-autoguiding system which uses scientific images for guiding.^{14–17} Specifically, the stellar centroids of several bright stars are measured on one of the three band images soon after the image is obtained. Then the mean stellar displacement on the latest image relative to a reference image is calculated to feed back to the telescope. All the above processes are done within a few seconds after the end of exposure. We note that the CCD channel to be used for the stellar centroid calculation is selectable. We usually set the exposure time for the guiding channel to 30 to 60 s such that the feedback result will be well reflected in the next image and that the guiding frequency is high enough. As shown in Sec. 4.4, the autoguiding system can stabilize the stellar centroid positions within ~ 1 pixel for bright stars (magnitude less than about 12). This is important for reducing systematic errors caused by the incompleteness of flat-fielding. We find no large difference in the autoguiding performance between in-focus and out-of-focus observations, meaning that the guiding performance is not limited by the degree of defocus, but is limited by the change of stellar point spread function (PSF) shapes due to the seeing variation and the mechanical accuracy of telescope drives (tracking and fine movements).

4 Results of Engineering Observations

We conducted the first light engineering observation on the night of December 24, 2014, and further engineering observations on the nights of March 2 to 4 and April 3 to 5, 2015. We examine the performance of MuSCAT using data taken on the nights. We summarize the results of the engineering observations below.

4.1 Detector Characteristics Including Bias, Flat, and Linearity

We have taken hundreds of bias, flat, and linearity test frames during engineering observations in order to learn the detector characteristics of MuSCAT. We have observed lights of a filament lamp projected onto a matte whiteboard on a wall of the 188-cm telescope dome for flat frames and linearity test frames. We do not find any strange features or significant bad pixel regions in the bias and flat frames, except a unique feature with a low etaloning process in the g'_2 and $z_{s,2}$ band flat images. For the reference, we present median flat images in the g'_2 (median of 433 flat frames) and r'_2 (median of 490 flat frames) bands in Fig. 12. We note that this unique feature has a very good repeatability with a fractional fluctuation of much less than 0.1%, which has little impact on the photometric precision required for our purposes. We have also exposed a very bright star of $V = 6$ to check for the existence of image persistence on the CCDs and ghost patterns due to reflection by the lenses. We found no apparent features that can affect the photometry. We have derived full well values, gains, and readout noises for the data. The values are presented in Table 1.

We have also tested the linearity of MuSCAT CCDs for each readout speed and each gain. Our method is based on a previous study for the CCDs with high-dispersion spectrograph of the Subaru telescope.¹⁹ First, we have created linearity test frames which have gradational counts on the CCDs, by opening only half of the tertiary mirror cover and inserting a black plate into the light path in front of MuSCAT. Figure 13 shows an example of a linearity test frame. Second, we monitor counts of the filament lamp until the filament lamp is stabilized. We note that it takes about 2 h until counts become nearly unchanged. We then start linearity test exposures as follows. We first determine an exposure time for each CCD which gives counts from the bias level to the saturation level gradationally on the CCDs. We define frames with the above exposure time as “A” frames

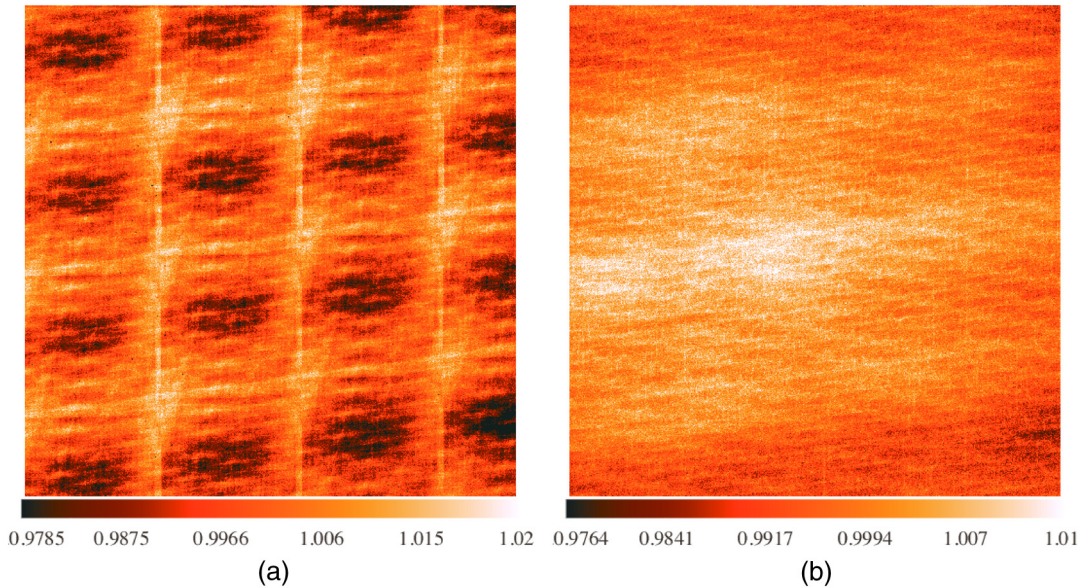


Fig. 12 Median flat images of (a) g'_2 band (with low etaloning process) and (b) r'_2 band (standard CCD).

and the frames with half of the exposure time as “ B ” frames. We then take A and B frames alternately until obtaining 20 frames each. We have repeated such exposures for each gain and each readout speed, namely for the gain modes of 1, 2, 4 e^- /ADU, and for the readout speeds of 100 kHz and 2 MHz. Subsequently, we subtract a median bias frame for each gain and each readout speed. We then make a new frame which computes the photon counts of each pixel in an A frame minus twice the photon counts for the same pixel in a B frame using adjacent A and B frames (39 pairs in total for each gain and each readout speed). We define those frames as “ C ” frames (namely, $C = A - 2 \times B$ for each pixel). To visualize the linearity of the CCDs,

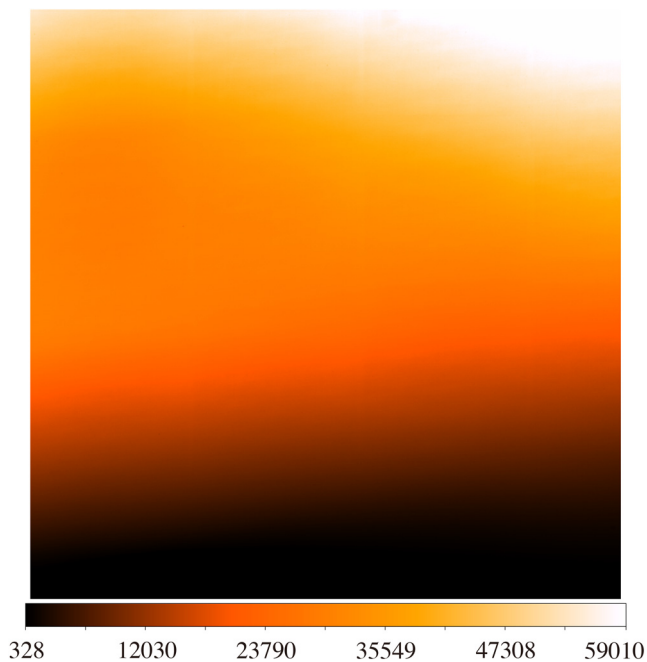


Fig. 13 An example of a linearity test frame in g'_2 band. Counts of the dark region are nearly bias level and those in the brightest region are saturated.

we plot electron counts (namely, photon counts \times gain) of pixels in A frames as the X -axis and electron counts of the same pixels in C frames as the Y -axis. An example of such a figure is shown in Fig. 14. We finally fit the plotted data with a linear function ($Y = aX$) using the data up to $X = 64,000$, and the best-fit linearity slopes are summarized in Table 3. Based on the above test, we have confirmed that MuSCAT CCDs have a good linearity within $\sim 0.21\%$ at a maximum up to the saturation level. The result means that the effect of nonlinearity is negligible even for high-precision transit photometry if the counts of stars do not change drastically during observations. In case we need to correct nonlinearity, we will use those data for nonlinearity corrections.

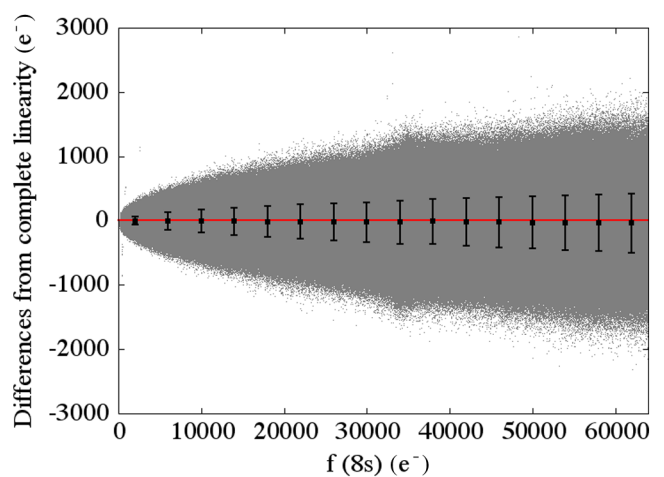


Fig. 14 An example of a result of a linearity test. The gray dots (about 40,000,000 points) represent the raw data. The horizontal axis [$f(8\text{ s})$ (e^-)] indicates electron counts in 8 s. The vertical axis shows the differences from complete linearity, which is defined as $f(8\text{ s}) - 2 * f(4\text{ s})$ (e^-). The black bars represent the mean and standard deviation for the raw data in segments with the horizontal width of 4000 electron counts.

Table 3 Summary of linearity information of CCDs for each gain and each readout speed.

Gain mode	ADC speed (Hz)	g'_2 -band linearity slope (%)	r'_2 -band linearity slope (%)	$z_{s,2}$ -band linearity slope (%)
1	2×10^6	0.154 ± 0.062	0.104 ± 0.051	0.204 ± 0.026
	1×10^5	-0.198 ± 0.071	-0.055 ± 0.043	-0.133 ± 0.040
2	2×10^6	0.016 ± 0.072	0.018 ± 0.045	0.112 ± 0.025
	1×10^5	-0.210 ± 0.069	0.005 ± 0.043	-0.061 ± 0.039
4	2×10^6	0.169 ± 0.044	0.120 ± 0.037	0.115 ± 0.030
	1×10^5	-0.059 ± 0.077	-0.085 ± 0.043	-0.037 ± 0.034

4.2 Point Spread Function and Distortion

We obtained images of the open cluster M67 with MuSCAT during the first light observation. On this night, the sky condition was photometric and there was no moon. The airmass of M67 was ~ 1.2 . Using the M67 images, we have derived PSF and the distortion of MuSCAT images using IRAF, PSFEx,²⁰

SExtractor,²¹ and SCAMP.²² The extracted PSF, its ellipticity, and FWHM of MuSCAT CCDs are shown in Figs. 15, 16, and 17, respectively. We note that we have used “PIXEL-AUTO” for the parameter of the PSF model in PSFEx. The software estimates a representative PSF for each grid using stars inside the grid. We also note that the seeings in g'_2 , r'_2 , and $z_{s,2}$ were 2.1, 1.8, and 1.7 in., respectively, which was slightly

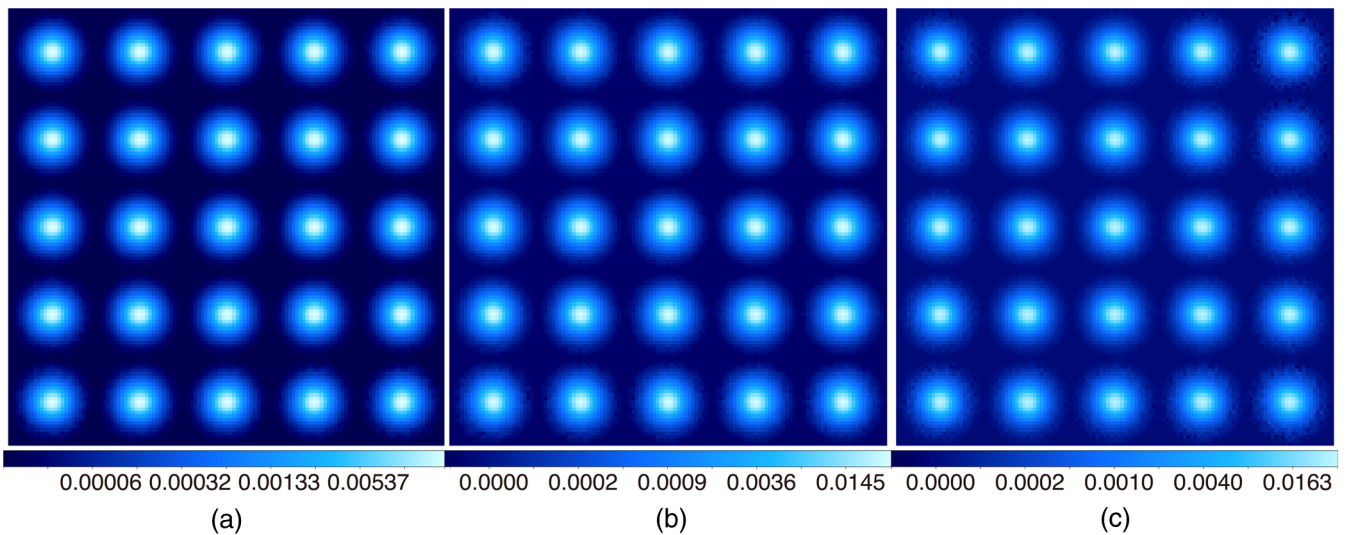


Fig. 15 Point spread function on the detectors extracted from M67 images in (a) g'_2 band, (b) r'_2 band, and (c) $z_{s,2}$ band.

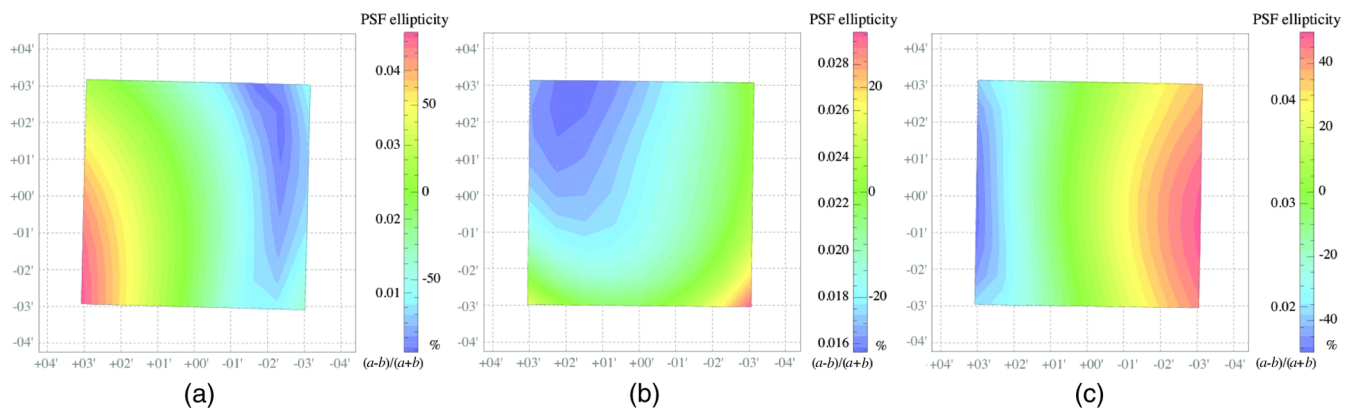


Fig. 16 Same as Fig. 15, but with ellipticity maps on the detectors.

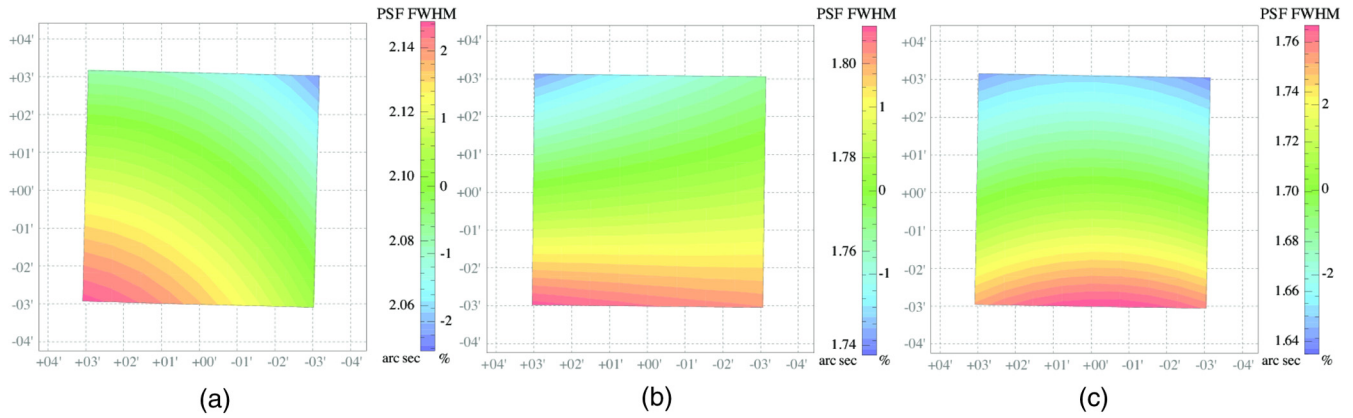


Fig. 17 Same as Fig. 15, but with FWHM maps on the detectors.

worse than the typical seeing at the site of ~ 1.5 in. in the optical bands. Thus, imaging quality was not limited by MuSCAT itself but by the seeing. We have confirmed that the PSF is nearly circular throughout the FOV and that MuSCAT does not have an unexpected large aberration or imaging problems.

We have also derived distortion maps of images as differences in the pixel scale on the CCDs using one of the output options of SCAMP.²³ The derived pixel scale distortion maps are presented in Fig. 18. This figure indicates that the pixel scale distortion is limited within about 0.3%, which is negligible for standard aperture photometry.

4.3 Sensitivity and Efficiency

We also estimate limiting magnitudes for the g'_2 , r'_2 , and $z_{s,2}$ bands using the images of M67. The measured sky brightnesses in g'_2 , r'_2 , and $z_{s,2}$ were $19.9 \text{ mag arc sec}^{-2}$, $19.5 \text{ mag arc sec}^{-2}$, and $18.7 \text{ mag arc sec}^{-2}$, respectively. For each band, $10 \times 60 \text{ s}$ images were obtained with dithering. We note that we used a high speed readout mode (2 MHz). We apply bias-flat correction and stellar position alignment to the data and stacked them into a single image for each band. We conduct photometry for ~ 100 stars on each stacked image by using the DoPHOT package,²⁴ which performs an analytical PSF fitting. The measured instrumental magnitudes of these stars were then compared to the SDSS 9 catalog²⁵ for photometric calibration. We note that we here ignore color terms and simply approximate that the g'_2 , r'_2 , and $z_{s,2}$ bands are identical to the g' , r' , and z' bands, respectively. Limiting magnitudes with 10-min exposures are

estimated as the signal-to-noise (S/N) ratio reaches 10, yielding $g'_{\text{lim}} = 21.7$, $r'_{\text{lim}} = 21.7$, and $z_{\text{lim}} = 19.8$. We note that z_{lim} is affected by higher readout noises in $z_{s,2}$ band (see Table 1) as we used the high speed readout mode. For the S/N calculation, we simply adopt the photometric errors returned by DoPHOT. We show a plot for SDSS magnitudes versus photometric errors in Fig. 19.

In addition, the total TP, including the airmass, 188-cm telescope, and MuSCAT is measured with the same data. We estimate the total TP as follows. First, we measure the zero-point magnitudes on the stacked M67 images as $ZP(g'_2) = 28.63$, $ZP(r'_2) = 28.71$, and $ZP(z_{s,2}) = 27.08$, which correspond to 10 electrons for all bands. Next, we estimate the expected incident flux coming from an astronomical object with the above magnitudes into the effective area of the primary mirror of the 188-cm telescope. Finally, comparing the expected flux with the detected one (10 electrons), we estimate the total TP in g'_2 , r'_2 , and $z_{s,2}$ bands as 20%, 28%, and 13%, respectively. The actual measured values are almost the same with expected values from the airmass, 188-cm telescope, and MuSCAT, as shown in Table 4.

4.4 High-Precision Photometry

In order to check for the photometric performance of MuSCAT, we observed two stars; GJ 436^{26,27} and WASP-12,²⁸ both hosting a transiting planet. Observations were carried out on March 2, 2015, UT, during out-of-transit phases for both targets. There was no cloud, but the sky level was relatively high due to a

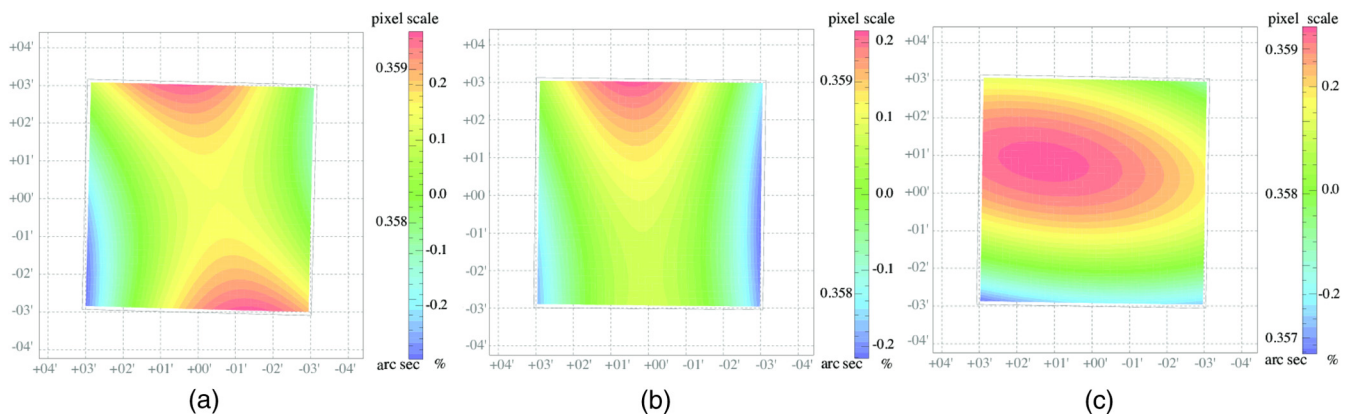


Fig. 18 Same as Fig. 15, but with pixel scale distortion maps on the detectors.

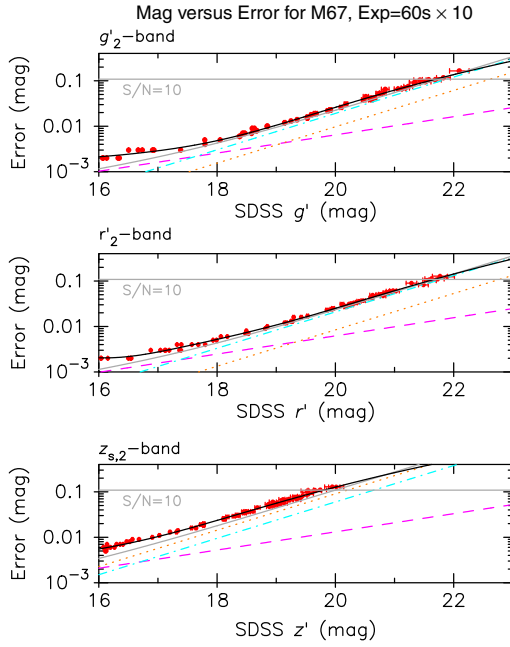


Fig. 19 Relations of SDSS magnitudes and photometric errors for M67 stars taken with MuSCAT. A dashed line in magenta, a dotted line in orange, a dashed-dotted line in cyan, and a solid line in gray represent the stellar photon noise, readout noise, sky photon noise, and total (theoretical) noise, respectively. The solid black line shows the best-fit fifth-order function, just for visibility.

bright waxing moon with an age (lunar phase) of 11.5. We used the low speed readout mode. GJ 436 is a nearby M3.5 dwarf with $g' = 11.81$, $r' = 10.08$, and $z' = 8.66$ in the SDSS magnitudes. GJ 436 was observed during 14:50 to 15:57 UT (airmass = 1.05–1.01) with an exposure time of 30 s for all bands. WASP-12 is a G0 dwarf with $B = 12.1$, $R = 11.2$ (from the NOMAD 1.0 catalog²⁹), and $z' = 11.41$.³⁰ WASP-12 was observed during 13:37 to 14:39 UT (airmass = 1.21–1.46) with an exposure time of 30 s (g'_2 and r'_2) or 60 s ($z'_{s,2}$). The exposure time and the number of exposures for each target and each filter is summarized in Table 5. For each observation, the FOV was adjusted so that several similar brightness stars were simultaneously imaged. The stellar image was defocused such that the FWHM of PSF became ~ 33 to ~ 38 pixels and ~ 31 to ~ 36 pixels for GJ 436 and WASP-12, respectively. The self-autoguiding

Table 4 Summary of throughput (TP) of MuSCAT on the 188-cm telescope at Okayama Astrophysical Observatory.

Band	Atmos. Transmittance (%)	M1 (%)		M2 (%)		Expected total TP (%)	
		M1 (%)	M2 (%)	MuSCAT (%)	total TP (%)	Measured TP (%)	
g'_2	$\sim 60^a$	86 ^b	79 ^b	51 ^d	21	20	
r'_2	$\sim 65^a$	85 ^b	85 ^b	56 ^d	27	28	
$z'_{s,2}$	$\sim 80^a$	$\sim 80^c$	$\sim 80^c$	29 ^d	15	13	

Note: M1 = main mirror, M2 = secondary mirror, MuSCAT = all optics \times BBAR coating \times QE.

^aTypical.

^bMeasured.

^cExpected.

^dExtrapolated from measured data up to 750 nm.

Table 5 Summary of the test observation and analysis.

Target (filter)	Exp. time (s)	N_{data}^a	N_{comp}^b	F_t/F_c^c	R_{ap}^d (pixel)	root-mean-square (rms) ^e (%)
GJ 436 (g'_2)	30	99	2	0.42	24	0.101
GJ 436 (r'_2)	30	99	3	0.85	26	0.074
GJ 436 ($z'_{s,2}$)	30	100	2	3.6	24	0.076
WASP-12 (g'_2)	30	79	4	0.38	22	0.16
WASP-12 (r'_2)	30	82	3	0.52	24	0.16
WASP-12 ($z'_{s,2}$)	60	45	2	0.59	22	0.15

^aThe number of observed data points.

^bThe number of comparison stars used for relative photometry.

^cUnnormalized flux ratio of the target star and the ensemble of the comparison stars.

^dApplied aperture radius.

^eThe rms value of the residual light curve from a linear fit.

system (see Sec. 3.2) was activated by using g'_2 band images for both targets. The stellar centroid changes in the r'_2 band during the observations of GJ 436 are displayed in Fig. 20, showing that the stellar positions were quite stable, with the dispersion not exceeding ~ 1 pixel.

The observed data were reduced by using a customized aperture-photometry pipeline.³¹ The applied aperture radius, the number of comparison stars used for the relative photometry, and the unnormalized flux ratio of the target star and the ensemble of the comparison stars are summarized in Table 5. Note that the applied aperture radius was determined such that the dispersion of the resultant light curve was minimum. We show the resultant normalized light curves of GJ 436 and WASP-12 in Figs. 21 and 22, respectively. The black dashed line indicates the best-fit linear function. Photometric precisions, which we define as the root-mean-square (rms) of the residual light curve from the linear fit to achieve 0.101%, 0.074%, and 0.076% in the g'_2 , r'_2 , and $z'_{s,2}$ bands for GJ 436, while those for WASP-12 are 0.16%, 0.16%, and 0.15%, respectively. These rms values are listed in Table 5.

To see how the photometric performance of MuSCAT has been achieved, we calculate the error budgets for these

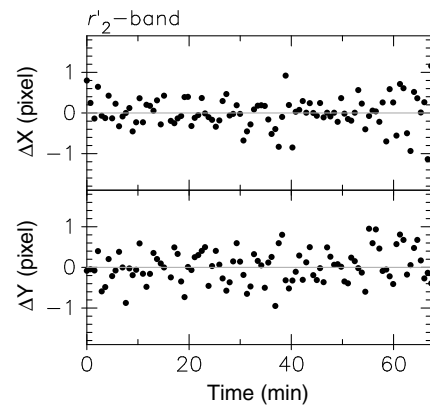


Fig. 20 Time series centroid positions of bright stars in the FOV for GJ 436.

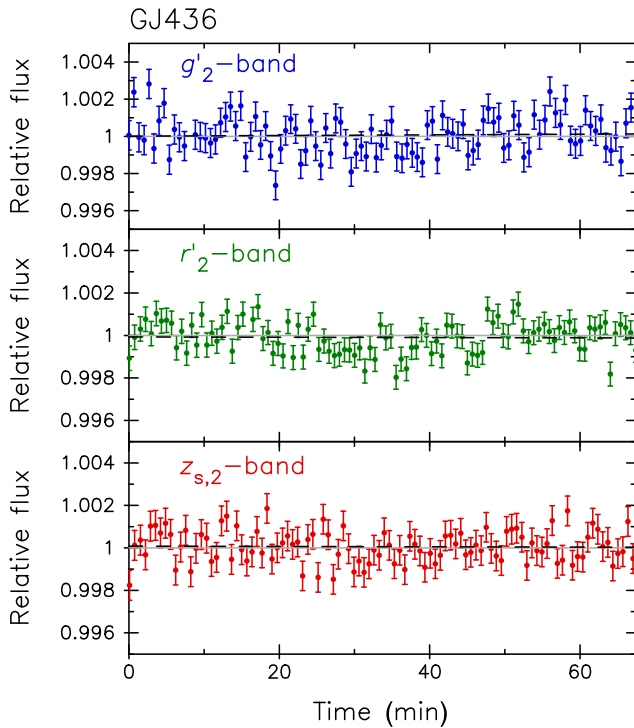


Fig. 21 Light curves of GJ 436.

observations as shown in Table 6. In this table, σ_{target} , σ_{comp} , and σ_{sky} indicate photon noises arising from the target-star flux, comparison-star flux, and sky-background flux, respectively, calculated assuming the Poisson (photon) noise. σ_{read} is the noise contributed from the read-out noise listed in Table 1. σ_{scin} is the scintillation noise, for which we apply the following equation:

$$\sigma_{\text{scin}} = 0.064D^{-2/3}(\text{sec } Z)^{7/4}e^{-h/h_0}T^{-1/2}, \quad (1)$$

where D is the diameter of the primary mirror of the telescope in cm, Z is the zenith distance, $h = 372$ m is the height above sea level of the observatory, $h_0 = 8000$ m, and T is the exposure time in seconds.^{32,33} All the remaining (unknown, or difficult to assess) components of the photometric error are treated as σ_{unknown} , which is calculated as

$$\sigma_{\text{unknown}} = \sqrt{\text{rms}^2 - \sigma_{\text{target}}^2 - \sigma_{\text{comp}}^2 - \sigma_{\text{sky}}^2 - \sigma_{\text{read}}^2 - \sigma_{\text{scin}}^2}, \quad (2)$$

Where the rms is the same as that listed in Table 5. Among these noise sources, all but σ_{unknown} are basically unavoidable. Possible causes of σ_{unknown} can be the difference of atmospheric transparency between toward the target star and toward the comparison stars, the modulation of scintillation noise, the incompleteness of flat-field correction, and so on. We find that σ_{unknown} is the major noise source in some of the light curves, but is still limited in degree to about 30% to 40% in rms^2 , meaning that σ_{unknown} is not a very limiting factor for the photometric precision. In other words, the greatest part of the photometric precision ($\geq 60\%$ in rms^2 for all three bands) can be explained by the theoretical noise models. We, therefore, consider that the expected photometric performance of MuSCAT has been well achieved.

We also note the time-correlated noise (the so-called ‘‘red’’ noise) in the observed data. For high-precision photometry such as transit observations, a treatment of the red noise would be very important.³⁴ We calculate a red-noise factor, which is the ratio of the measured rms in the binned data to the one expected from the rms in the unbinned data, for our observations. We find 1.3 on average, which is a typical value for ground-based transit observations. Although 1-h observations are not sufficient to evaluate the red noise in detail, we consider that the level of the red noise of MuSCAT is similar to other ground-based instruments. We will thus take into account the red noise for future science observations with MuSCAT.

5 Upgrading and Transferring Capability

Although the current MuSCAT is ready for operation, it still has upgrading capabilities. First, MuSCAT can be upgraded in terms of FOV by replacing the three $1\text{k} \times 1\text{k}$ CCD cameras, which give 6.1×6.1 arc min² FOV, with $2\text{k} \times 2\text{k}$ CCD cameras, which will provide 12.7×12.7 arc min² FOV. Such a wider FOV would be desirable to find good comparison stars, especially for very bright targets which will be discovered by the TESS mission. Second, MuSCAT has space for another dichroic mirror to add NIR channels (see Sec. 2.2). Additional NIR channels enable us to simultaneously take images from optical to NIR, like GROND. Such a capability will enhance the scientific merits for transmission spectroscopy in the light of efficiency and simultaneity.

MuSCAT also has a transferring capability. The current instrument is optimized for the 188-cm telescope at OAO whose F-number is F18, but MuSCAT can be transferred to or can make a copy of itself for other telescopes by replacing the F conversion lenses.

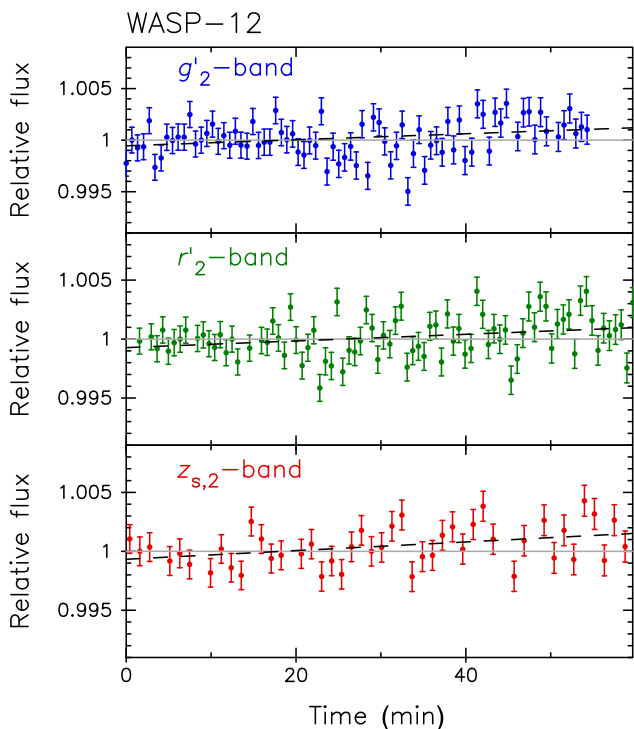


Fig. 22 Same as Fig. 21, but for WASP-12.

Table 6 Error budget.

Target (filter)	σ_{target} (%)	σ_{comp} (%)	σ_{sky} (%)	σ_{read} (%)	σ_{scin} (%)	σ_{unknown} (%)	rms (%)
WASP-12 (g'_2)	0.058	0.036	0.092^a	00.005	00.078	00.076	0.16
WASP-12 (r'_2)	0.047	0.034	0.077	0.004	0.081	0.106^a	0.16
WASP-12 ($z_{s,2}$)	0.065	0.048	0.083^a	0.006	0.057	0.083^a	0.15
GJ 436 (g'_2)	0.043	0.028	0.037	0.003	0.050	0.061^a	0.101
GJ 436 (r'_2)	0.023	0.021	0.019	0.001	0.050^a	0.041	0.074
GJ 436 ($z_{s,2}$)	0.023	0.043	0.023	0.003	0.050^a	0.019	0.076

^aThe bold text indicates the most dominant noise component for each light curve.

6 Summary

We have developed a new astronomical instrument MuSCAT for the 188-cm telescope at OAO in Japan. MuSCAT has a capability of three-color simultaneous imaging in the g'_2 (400 to 550 nm), r'_2 (550 to 700 nm), and $z_{s,2}$ (820 to 920 nm) bands with three $1\text{k} \times 1\text{k}$ pixel CCDs. The FOV of MuSCAT is 6.1×6.1 arc min² with a pixel scale of 0.358 arc sec/pixel.

One of the primary aims of MuSCAT is to confirm whether candidates of transiting planets discovered by transit surveys, including such as K2, TESS, and PLATO, are truly planets or false positives due to eclipsing binaries. Another primary aim of MuSCAT is to measure the wavelength dependence of transit depths in visible bands, providing rough information about exoplanetary atmospheres: such as the feature of the Rayleigh scattering by hydrogen dominated atmospheres, the feature of the Mie scattering by hazy atmospheres, or the flat feature of cloudy atmospheres.^{16,35}

The capability of multicolor simultaneous transit photometry is very suitable for those aims. Since MuSCAT can achieve a 0.1% photometric precision with a 30-s exposure for stars brighter than ~ 10 mag as shown in Sec. 4.4, MuSCAT will work especially effectively for the purposes of observing bright TESS transiting planets. In addition, MuSCAT would also be useful for follow-up observations of supernovae and gamma-ray bursts, and monitoring variable stars, and so on. The instrument is ready for operation at OAO.

Acknowledgments

We are very grateful for kind help by the staffs of Okayama Astrophysical Observatory, Astrobiology Center, and Exoplanet Detection Project Office in NAOJ. We acknowledge the following people, who helped us to obtain a research grant to develop this instrument: Masahiro Ikoma, Yui Kawashima, Bun'ei Sato, Yasuhito Sekine, Hidenori Genda, Takahiro Nagayama, Keigo Enya, and Mikio Kurita. N.N. acknowledges the support by the NAOJ Fellowship, Inoue Science Research Award, NINS Program for Cross-Disciplinary Study, and Grant-in-Aid for Scientific Research (A) (JSPS KAKENHI Grant No. 25247026). A.F. is supported by the Astrobiology Project of the Center for Novel Science Initiatives (CNSI), National Institutes of Natural Sciences (NINS) (Grant No. AB261005). N.K. is supported by the NINS Program for

Cross-Disciplinary Study. M.T. was partly supported by the JSPS KAKENHI Grant No. 22000005.

References

1. G. Á. Bakos et al., “HAT-P-1b: a large-radius, low-density exoplanet transiting one member of a stellar binary,” *Astrophys. J.* **656**, 552–559 (2007).
2. A. C. Cameron et al., “WASP-1b and WASP-2b: two new transiting exoplanets detected with SuperWASP and SOPHIE,” *Mon. Not. R. Astron. Soc.* **375**, 951–957 (2007).
3. R. J. Siverd et al., “KELT-1b: a strongly irradiated, highly inflated, short period, 27 Jupiter-mass companion transiting a mid-F star,” *Astrophys. J.* **761**, 123 (2012).
4. A. Baglin et al., “CoRoT: a high precision photometer for stellar evolution and exoplanet finding,” in *36th COSPAR Scientific Assembly, COSPAR, Plenary Meeting*, Vol. 36, pp. 3749 (2006).
5. W. J. Borucki et al., “Kepler planet-detection mission: introduction and first results,” *Science* **327**, 977 (2010).
6. S. B. Howell et al., “The K2 mission: characterization and early results,” *Publ. Astron. Soc. Pac.* **126**, 398–408 (2014).
7. G. R. Ricker et al., “Transiting Exoplanet Survey Satellite (TESS),” *J. Astron. Telesc. Instrum. Syst.* **1**(1), 014003 (2015).
8. H. Rauer et al., “The PLATO 2.0 mission,” *Exp. Astron.* **38**, 249–330 (2014).
9. K. D. Colón, E. B. Ford, and R. C. Morehead, “Constraining the false positive rate for Kepler planet candidates with multicolour photometry from the GTC,” *Mon. Not. R. Astron. Soc.* **426**, 342–353 (2012).
10. N. Nikolov et al., “Refined physical properties and g' , r' , i' , z' , J, H, K transmission spectrum of WASP-23b from the ground,” *Astron. Astrophys.* **553**, A26 (2013).
11. L. Mancini et al., “Physical properties, transmission and emission spectra of the WASP-19 planetary system from multi-colour photometry,” *Mon. Not. R. Astron. Soc.* **436**, 2–18 (2013).
12. L. Mancini et al., “Physical properties, star-spot activity, orbital obliquity and transmission spectrum of the Qatar-2 planetary system from multicolour photometry,” *Mon. Not. R. Astron. Soc.* **443**, 2391–2409 (2014).
13. J. Bento et al., “Optical transmission photometry of the highly inflated exoplanet WASP-17b,” *Mon. Not. R. Astron. Soc.* **437**, 1511–1518 (2014).
14. N. Narita et al., “IRSF SIRIUS JHK_s simultaneous transit photometry of GJ 1214b,” *Publ. Astron. Soc. Jpn.* **65**, 27 (2013).
15. N. Narita et al., “Multi-color transit photometry of GJ 1214b through BJHK_s bands and a long-term monitoring of the stellar variability of GJ 1214,” *Astrophys. J.* **773**, 144 (2013).
16. A. Fukui et al., “Optical-to-near-infrared simultaneous observations for the hot Uranus GJ3470b: a hint of a cloud-free atmosphere,” *Astrophys. J.* **770**, 95 (2013).
17. A. Fukui et al., “Multi-band, multi-epoch observations of the transiting warm Jupiter WASP-80b,” *Astrophys. J.* **790**, 108 (2014).

18. J. Southworth et al., “High-precision photometry by telescope defocusing—I. The transiting planetary system WASP-5,” *Mon. Not. R. Astron. Soc.* **396**, 1023–1031 (2009).
 19. A. Tajitsu et al., “Nonlinearity in the detector used in the Subaru telescope high dispersion spectrograph,” *Publ. Natl. Astron. Obs. Jpn.* **13**, 1–8 (2010).
 20. E. Bertin, “Automated Morphometry with SExtractor and PSFEX,” in *Astronomical Data Analysis Software and Systems XX*, I. N. Evans et al., Eds., Astronomical Society of the Pacific Conference Series, Vol. **442**, pp. 435, Astronomical Society of the Pacific, San Francisco (2011).
 21. E. Bertin and S. Arnouts, “SExtractor: software for source extraction,” *Astron. Astrophys.* **117**, 393–404 (1996).
 22. E. Bertin, “Automatic astrometric and photometric calibration with SCAMP,” in *Astronomical Data Analysis Software and Systems XV*, C. Gabriel et al., Eds., Astronomical Society of the Pacific Conference Series, Vol. **351**, pp. 112, Astronomical Society of the Pacific, San Francisco (2006).
 23. M. R. Calabretta et al., “Representations of distortions in FITS world coordinate systems,” in *Astronomical Data Analysis Software and Systems (ADASS) XIII*, F. Ochsenbein, M. G. Allen, and D. Egret, Eds., Astronomical Society of the Pacific Conference Series, Vol. **314**, pp. 551, Astronomical Society of the Pacific, San Francisco (2004).
 24. P. L. Schechter, M. Mateo, and A. Saha, “DOPHOT, a CCD photometry program: description and tests,” *Publ. Astron. Soc. Pac.* **105**, 1342–1353 (1993).
 25. C. P. Ahn et al., “The ninth data release of the Sloan digital sky survey: first spectroscopic data from the SDSS-III baryon oscillation spectroscopic survey,” *Astrophys. J. Suppl. Ser.* **203**, 21 (2012).
 26. R. P. Butler et al., “A Neptune–Mass planet orbiting the nearby M Dwarf GJ 436,” *Astrophys. J.* **617**, 580–588 (2004).
 27. M. Gillon et al., “Detection of transits of the nearby hot Neptune GJ 436 b,” *Astron. Astrophys.* **472**, L13–L16 (2007).
 28. L. Hebb et al., “WASP-12b: the hottest transiting extrasolar planet yet discovered,” *Astrophys. J.* **693**, 1920–1928 (2009).
 29. N. Zacharias et al., “The Naval Observatory Merged Astrometric Dataset (NOMAD),” in *American Astronomical Society Meeting Abstracts, Bulletin of the American Astronomical Society* **36**, 1418 (2004).
 30. C. Bergfors et al., “Stellar companions to exoplanet host stars: lucky imaging of transiting planet hosts,” *Mon. Not. R. Astron. Soc.* **428**, 182–189 (2013).
 31. A. Fukui et al., “Measurements of transit timing variations for WASP-5b,” *Publ. Astron. Soc. Jpn.* **63**, 287 (2011).
 32. A. T. Young, “Photometric error analysis. VI. Confirmation of Reiger’s theory of scintillation,” *Astron. J.* **72**, 747 (1967).
 33. D. Dravins et al., “Atmospheric intensity scintillation of stars. III. Effects for different telescope apertures,” *Publ. Astron. Soc. Pac.* **110**, 610–633 (1998).
 34. F. Pont, S. Zucker, and D. Queloz, “The effect of red noise on planetary transit detection,” *Mon. Not. R. Astron. Soc.* **373**, 231–242 (2006).
 35. A. R. Howe and A. S. Burrows, “Theoretical transit spectra for GJ 1214b and other super-Earths,” *Astrophys. J.* **756**, 176 (2012).
- Norio Narita** is the principal investigator of the MuSCAT instrument and its observing team. He is jointly appointed from Astrobiology Center, National Astronomical Observatory of Japan, and SOKENDAI (The Graduate University of Advanced Studies) as a research assistant professor.

Biographies for the other authors are not available.